The Astrophysical Journal Letters, 956:L45 (13pp), 2023 October 20 https://doi.org/10.3847/2041-8213/ad01bd

An SiO Toroid and Wide-angle Outflow Associated with the Massive Protostar W75N (B)-VLA2

José F. Gómez[1], José M. Torrelles[2,3], Josep M. Girart[2,3], Gabriele Surcis[4], Jeong-Sook Kim[5,6], Jorge Cantó[7], Guillem Anglada[1], Salvador Curiel[7], Wouter H. T. Vlemmings[8], Carlos Carrasco-González[9], Adriana R. Rodríguez-Kamenetzky[10], Soon-Wook Kim[6], Ciriaco Goddi[4,11,12,13], Huib J. van Langevelde[14,15], and Álvaro Sanchez-Monge[2,3]

[1] Instituto de Astrofísica de Andalucía (IAA-CSIC), Glorieta de la Astronomía s/n, E-18008 Granada, Spain; jfg@iaa.es
[2] Institut de Ciències de l'Espai (ICE-CSIC), Can Magrans s/n, E-08193, Bellaterra, Barcelona, Spain
[3] Institut d'Estudis Espacials de Catalunya (IEEC), Barcelona, Spain
[4] INAF—Osservatorio Astronomico di Cagliari, Via della Scienza 5, I-09047, Selargius, Italy
[5] National Astronomical Observatories, Chinese Academy of Sciences, 20A Datun Road, Chaoyang District, Beijing, People's Republic of China
[6] Korea Astronomy and Space Science Institute, 776 Daedeokdaero, Yuseong, Daejeon 305-348, Republic of Korea
[7] Instituto de Astronomía, Universidad Nacional Autónoma de México (UNAM), Apdo Postal 70-264, México, D.F., Mexico
[8] Department of Space, Earth and Environment, Chalmers University of Technology, Onsala Space Observatory, SE-439 92, Sweden
[9] Instituto de Radioastronomía y Astrofísica (IRyA-UNAM), Morelia, Mexico
[10] Instituto de Astronomía Teórica y Experimental (IATE, CONICET-UNC), Córdoba, Argentina
[11] Instituto de Astronomia, Geofísica e Ciências Atmosféricas, Universidade de São Paulo, São Paulo, SP 05508-090, Brazil
[12] Dipartimento di Fisica, Universitá degli Studi di Cagliari, SP Monserrato-Sestu km 0.7, I-09042 Monserrato (CA), Italy
[13] INFN, Sezione di Cagliari, I-09042 Monserrato (CA), Italy
[14] Joint Institute for VLBI ERIC, Oude Hoogeveensedijk 4, 7991 PD Dwingeloo, The Netherlands
[15] Sterrewacht Leiden, Leiden University, Postbus 9513, 2300 RA Leiden, The Netherlands
Received 2023 September 21; revised 2023 October 9; accepted 2023 October 10; published 2023 November 3

Abstract

We have carried out Atacama Large Millimeter/submillimeter Array observations of the massive star-forming region W75N(B), which contains the massive protostars VLA1, VLA2, and VLA3. Particularly, VLA2 is an enigmatic protostar associated with a wind-driven H_2O maser shell, which has evolved from an almost isotropic outflow to a collimated one in just 20 yr. The shell expansion seemed to be halted by an obstacle located to the northeast of VLA2. Here we present our findings from observing the 1.3 mm continuum and H_2CO and SiO emission lines. Within a region of ∼30″ (∼39,000 au) diameter, we have detected 40 compact millimeter continuum sources, three of them coinciding with VLA1, VLA2, and VLA3. While the H_2CO emission is mainly distributed in a fragmented structure around the three massive protostars, but without any of the main H_2CO clumps spatially coinciding with them, the SiO is highly concentrated on VLA2, indicating the presence of very strong shocks generated near this protostar. The SiO emission is clearly resolved into an elongated structure (∼0.″6 × 0.″3; ∼780 au × 390 au) perpendicular to the major axis of the wind-driven maser shell. The structure and kinematics of the SiO emission are consistent with a toroid and a wide-angle outflow surrounding a central mass of $\sim 10\,M_{\odot}$, thus supporting previous theoretical predictions regarding the evolution of the outflow. Additionally, we have identified the expected location and estimated the gas density of the obstacle that is hindering the expansion of the maser shell.

Unified Astronomy Thesaurus concepts: Protostars (1302); Stellar jets (1607); Radio continuum emission (1340); Circumstellar disks (235); Stellar winds (1636); Star forming regions (1565)

1. Introduction

Understanding how massive stars form and evolve remains a major challenge in astrophysics. One of the observational approaches to advance in this field has been to search for systems with disks and jets in massive protostars deeply embedded in their parental molecular clouds, trying to find similarities with the formation and evolution of low-mass stars. Thus, several disk-jet systems in massive protostars are known today, indicating that they likely form in a similar way to low-mass stars, following the so-called monolithic core-accretion model, e.g., Cep A HW2 (Patel et al. 2005; Jiménez-Serra et al. 2007; Sanna et al. 2017) and HH 80-81 (Girart et al. 2018; Añez-López et al. 2020). However, in the last few years, several observational studies have indicated that during the early stages of the evolution of massive protostars, there may be episodic events of short duration (tens of years) associated with very poorly collimated or near-isotropic outflows (e.g., Torrelles et al. 2001; Kim et al. 2013; Surcis et al. 2014; Carrasco-González et al. 2015; Bartkiewicz et al. 2020). These results are surprising since, according to the core-accretion model, collimated outflows are already expected in the earliest phases of star formation, rather than outflows that expand without any preferential direction. This expectation has been also confirmed with high-resolution observations of high-mass protostars in clustered star-forming regions (e.g., Goddi et al. 2020). Therefore, it is still an open question whether the collimation and mass-ejection mechanisms in the early life of massive protostars differ from the case of low-mass protostars (see, e.g., Carrasco-González et al. 2021). This has important consequences for having a global vision of star formation since

mass ejection is related to the accretion process and then to the evolution of the protostar to its final mass.

A very enigmatic case is the massive protostar W75N(B)-VLA2. Through a research program consisting of monitoring for more than 20 yr an expanding water-vapor maser shell and the radio continuum emission associated with this source, it has been possible to observe the transformation of a short-lived, originally poorly collimated outflow from a massive protostar into a collimated jet, as reported by Carrasco-González et al. (2015). This sudden change of the outflow morphology has been modeled by these authors in terms of an episodic, short-lived, originally isotropic, ionized wind that drives the observed maser shell around VLA2 and whose morphology evolves as a consequence of the interaction with a toroidal density stratification. However, these expanding motions are not symmetric because they seem to be halted by a possible dense obstacle at a distance of $\sim 0\farcs2$ to the northeast of VLA2, as recently suggested by Surcis et al. (2023) through a monitoring of the H_2O maser emission with the European very long baseline interferometry (VLBI) Network (EVN). A detailed description of the main properties of VLA2, as well as those of the other massive protostars in the high-mass star-forming region W75N(B), which is located at a distance of 1.3 kpc (Rygl et al. 2012), can be found in Surcis et al. (2023).

In this work, we present Atacama Large Millimeter/submillimeter Array (ALMA) continuum and H_2CO and SiO line observations at 1.3 mm wavelength toward the brightest millimeter core of the W75N(B) region, MM1 (Shepherd 2001; Minh et al. 2010; Rodríguez-Kamenetzky et al. 2020; van der Walt et al. 2021), which contains the massive protostars VLA1, VLA2, and VLA3 seen at radio continuum wavelengths (Hunter et al. 1994; Torrelles et al. 1997; Rodríguez-Kamenetzky et al. 2020). These protostars have individual masses equivalent to B1-B0.5 spectral type stars (e.g., Shepherd 2001). The main goal of our ALMA observations was to test the presence of the molecular toroid around VLA2 predicted by previous works (Carrasco-González et al. 2015), as well as to study the distribution of gas and dust in the environment of these massive protostars. In a forthcoming paper, we will analyze the emission from the other multiple molecular lines detected in this very active high-mass star-forming region.

2. Observations

The ALMA observations in Band 6 ($\lambda = 1.1$–1.4 mm; project 2019.1.00059.S; PI: Jeong-Sook Kim) were performed on four different sessions, and using two different array configurations: configuration C43-5 on 2021 April 29 (baselines 14–1261 m) and 2022 August 2 (baselines 15–1301 m), and configuration C43-8 on 2021 August 18 (baselines 92–8282 m) and 2021 October 28 (baselines 63–8282 m). The average observing time per session was ∼45 minutes, including calibration. The source J0006-0623 was used as a flux and bandpass calibrator, while J2007+4029 was used as a complex gain calibrator. The pointing position for the target W75N(B)-VLA2 was $\alpha(\mathrm{J2000}) = 20^{\mathrm{h}}38^{\mathrm{m}}36\fs486$, $\delta(\mathrm{J2000}) = 42°37'34\farcs09$. The spectral setup consisted of six spectral windows with different bandwidths (BW) and velocity resolutions (ΔV_{ch}), five of them centered on the rest frequencies (RF) of the molecular lines H_2CO [3(0,3)-2(0,2)], SiO [$v = 0$, 5-4], $C^{18}O$ [2-1], ^{13}CO [2-1], ^{12}CO [2-1], plus a continuum bandwidth (see Table 1). The ALMA data were pipeline calibrated, reduced, and analyzed with CASA version 6.2.1.7 (CASA Team et al. 2022). The continuum data (obtained from line free-channels of the spectral windows plus the continuum spectral window) were self-calibrated and their solutions were also applied to the spectral line data. For imaging, we used task tclean of CASA, with a Brigg's weighting of visibilities, and a robust parameter of 0.5 (unless otherwise noted), resulting in a synthesized beam of $\sim 0\farcs17 \times 0\farcs08$ (PA $\simeq -2°$). A high dynamic range for the continuum image of ∼1100 (rms = 0.08 mJy beam^{-1}) was reached after self-calibration (Figure 1). Images presented in this paper were corrected by the primary beam response, which has an FWHM of $\simeq 25''$ at 230 GHz.

Table 1
Spectral Setup

Spectral Window	RF (GHz)	BW (MHz)	ΔV_{ch} (km s^{-1})
H_2CO [3(0,3)-2(0,2)]	218.222192	468.75	0.775
SiO [$v = 0$, 5-4]	217.104980	468.75	0.779
$C^{18}O$ [2-1]	219.560358	234.38	0.385
^{13}CO [2-1]	220.398684	234.38	0.384
^{12}CO [2-1]	230.538000	468.75	0.734
Continuum	231.805970	1,875	40.443

3. Results

3.1. Dust Continuum Emission

Figure 1 shows the continuum image obtained toward the central part of the W75N(B) region. The millimeter cores MM1, MM2, and MM3 (previously observed with a beam of $\simeq 1''$–$2''$; Minh et al. 2010; Rodríguez-Kamenetzky et al. 2020; van der Walt et al. 2021), are now resolved into multiple compact millimeter sources. All known radio continuum sources at centimeter wavelengths in this region (labeled and indicated by crosses in Figure 1; from Rodríguez-Kamenetzky et al. 2020), except Bc[E], Bc[W], Bd, and VLA4, have associated continuum emission at millimeter wavelengths, further reinforcing that VLA1, VLA2, VLA3, VLA[SW], and VLA[NE] are embedded protostars. The FWHM of these continuum sources is unresolved by our beam. On the other hand, the fact that Bc[E], Bc[W], Bd, and VLA4 have no continuum emission at millimeter wavelengths (Figure 1) gives support to the interpretation by Carrasco-González et al. (2010) and Rodríguez-Kamenetzky et al. (2020), through proper motion measurements, that these four objects are not embedded protostars, but obscured Herbig–Haro (HH) objects excited by the massive protostar VLA3.

In order to better distinguish weak compact millimeter continuum sources from extended emission present in the region (see Figure 1), we obtained images that exclude baselines shorter than 200 kλ, thus filtering out large-scale structures, in a similar way as in Girart et al. (2018) and Busquet et al. (2019). With this baseline restriction, 40 unresolved continuum sources have been identified in a region of $\sim 30''$ (∼39,000 au) diameter centered on VLA2, and with flux densities in the range of ∼0.4–90 mJy beam^{-1} (Table A1, Figure A1). We are proposing, in particular, that one of these detected sources (ID 32 in Table A1) is the powering source of the highly collimated bipolar jet that we have detected $\sim 6''$ (∼7800 au) northeast of VLA2 (see Appendix C and

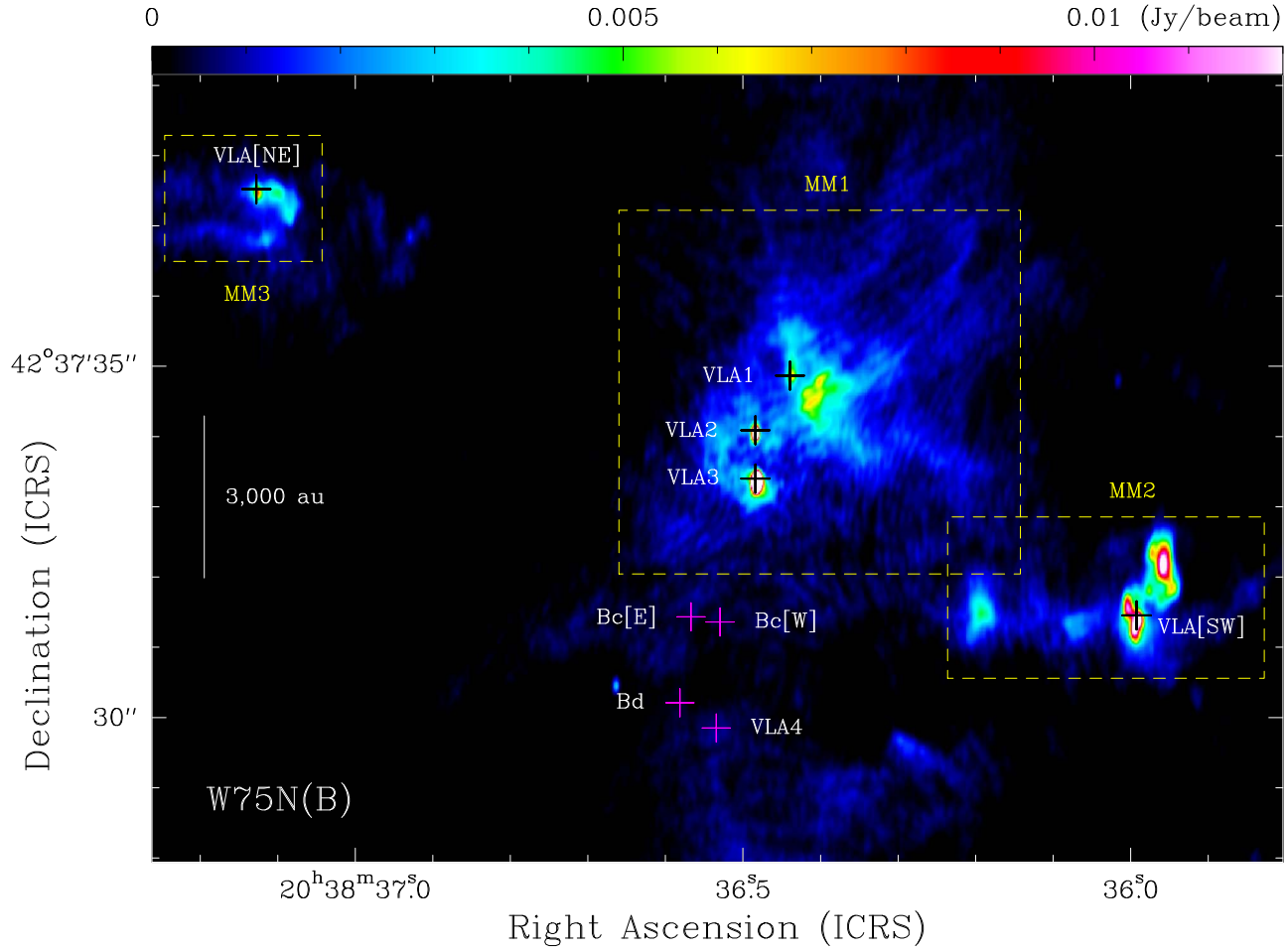

Figure 1. ALMA 1.3 mm continuum emission image of the high-mass star-forming region W75N(B). The intensity range of the image has been saturated at 15 mJy beam^{-1} (beam = $0\farcs17 \times 0\farcs08$, PA = $-2°$; rms $\simeq$0.08 mJy beam^{-1}) to distinguish the faintest continuum sources, given the high dynamic range of the image ($\sim$1100). The maximum of the image (coincident with VLA3) is 97 mJy beam^{-1}. The position of the radio continuum sources detected in the region at centimeter wavelengths, including the massive protostars VLA1, VLA2, and VLA3, are labeled and indicated by crosses, while dotted rectangles indicate the regions MM1, MM2, and MM3 where continuum emission was previously reported at 1.3 mm with ALMA, but with a beam of $1\farcs73 \times 0\farcs86$, PA = $-4°$ (Rodríguez-Kamenetzky et al. 2020). Table A1 lists the positions of all the millimeter continuum sources detected in the region (see Section 3.1, Appendix A, and Figure A1).

Figure C1), and that will be discussed in detail in a forthcoming paper.

3.2. H_2CO Line Emission

The emission of the formaldehyde molecule is known to be a good tracer of dense gas ($n[H_2] \gtrsim 5 \times 10^5$–$10^6$ cm^{-3}) over a wide range of temperatures ($T_K \simeq$ 10–300 K) in the cores of molecular clouds (e.g., Mangum & Wootten 1993; Shirley 2015). The integrated emission image obtained from the H_2CO [3(0,3)-2(0,2)] line in the velocity range $V_{LSR} \simeq -4$ to $+23$ km s^{-1} (Figure 2(a)) shows a clumpy structure over a plateau of relatively weak emission covering a region of $\sim 3-4''$ ($\sim$3900–5200 au). None of the main H_2CO clumps coincide with the position of any of the massive protostars VLA1, VLA2, or VLA3. The velocity field of the H_2CO emission (Figure 2(b)) shows that the greatest velocity differences are found along the northwest–southeast direction at angular scales of $\sim 3''$ ($\sim$3900 au), with blueshifted ($V_{LSR} \simeq +6$ km s^{-1}) and redshifted velocities ($V_{LSR} \simeq +13$ km s^{-1}) to the northwest and southeast of VLA2, respectively (ambient velocity $V_{LSR} \simeq +10$ km s^{-1}; e.g., Surcis et al. 2023). This direction also coincides with the orientation of the strongest H_2CO emission (Figure 2(b)) and is consistent with the velocity field previously observed with the Submillimeter Array (SMA) and ALMA through different molecular species (e.g., H_2CO, CS, SO_2, CH_3OH), at scales of $\sim 4''$ and angular resolutions of $\sim 1'' - 2''$ (Minh et al. 2010; Rodríguez-Kamenetzky et al. 2020; van der Walt et al. 2021). In particular, van der Walt et al. (2021) suggested that the observed velocity shift is due to infalling gas onto a disk-like structure surrounding one of the massive protostars, but without being able to specify which one, probably due to an insufficient angular resolution in their observations ($\sim 1''$). More recently, Zeng et al. (2023) concluded that the gas infall proceeds along the magnetic field lines, as the gravitational force dominates over the magnetic field.

We suggest that the distribution of the clumpy H_2CO structure near but around VLA1, VLA2, and VLA3 could be due either to residual dense molecular gas fragments after the formation of these massive protostars, or to material still infalling toward the center of the region. This is supported by the fact that none of the main H_2CO clumps observed around the massive protostars have an associated millimeter continuum source (see Figures A1, 2(a), Table A1). The clumps observed in H_2CO have a relatively low mass of gas. For example, for the most intense clump (located $\sim 0\farcs2$–$0\farcs3$ northeast of

Table A1
ALMA 1.3 mm Continuum Sources Detected in the W75N(B) Field[a]

Source ID	R.A. (J2000)	Decl. (J2000)	S_ν (mJy beam^{-1})[b]	Δd (arcsec)[c]	M_J[d]	Association[e]
1	20 38 35.375	42 37 13.75	21.36	23.75	313	⋯
2	20 38 35.671	42 37 31.39	2.45	9.39	36	⋯
3	20 38 35.769	42 37 50.41	3.76	18.14	55	⋯
4	20 38 35.837	42 37 26.82	0.94	10.21	14	⋯
5	20 38 35.947	42 37 31.86	3.39	6.35	50	MM2
6	20 38 35.959	42 37 32.17	8.24	6.13	121	MM2
7	20 38 35.974	42 37 32.35	3.87	5.91	57	MM2
8	20 38 35.977	42 37 31.82	1.83	6.06	27	MM2
9	20 38 35.991	42 37 31.39	12.68	6.09	186	MM2, VLA[SW]
10	20 38 36.004	42 37 31.57	6.66	5.89	98	MM2
11	20 38 36.016	42 37 34.79	1.02	5.23	15	⋯
12	20 38 36.025	42 37 27.29	0.75	8.49	11	⋯
13	20 38 36.036	42 37 27.37	0.75	8.36	11	⋯
14	20 38 36.070	42 37 31.35	0.75	5.35	11	MM2
15	20 38 36.080	42 37 31.35	0.85	5.25	12	MM2
16	20 38 36.194	42 37 31.47	1.88	4.15	28	MM2
17	20 38 36.270	42 37 29.54	0.65	5.14	10	⋯
18	20 38 36.279	42 37 29.60	0.78	5.04	11	⋯
19	20 38 36.287	42 37 29.64	0.86	4.96	13	⋯
20	20 38 36.298	42 37 29.70	1.05	4.86	15	⋯
21	20 38 36.302	42 37 23.61	4.24	10.67	62	⋯
22	20 38 36.401	42 37 34.79	2.16	1.17	32	MM1
23	20 38 36.414	42 37 34.40	1.95	0.85	29	MM1
24	20 38 36.418	42 37 34.63	1.60	0.92	23	MM1
25	20 38 36.437	42 37 34.86	3.32	0.94	49	MM1, VLA1
26	20 38 36.471	42 37 43.87	0.39	9.78	6	MM[N]
27	20 38 36.482	42 37 33.36	86.93	0.73	1275	MM1, VLA3
28	20 38 36.484	42 37 34.04	20.75	0.05	51[d]	MM1, VLA2
29	20 38 36.641	42 37 25.93	0.99	8.34	15	⋯
30	20 38 36.663	42 37 30.45	2.94	4.13	43	⋯
31	20 38 36.912	42 37 37.03	0.55	5.55	8	⋯
32	20 38 36.930	42 37 36.83	1.02	5.61	15	f
33	20 38 36.946	42 37 25.95	1.25	9.59	18	⋯
34	20 38 37.083	42 37 37.13	1.87	7.26	27	MM3
35	20 38 37.097	42 37 37.45	2.08	7.53	30	MM3
36	20 38 37.114	42 37 36.79	1.26	7.44	18	MM3
37	20 38 37.124	42 37 37.46	5.25	7.81	77	MM3, VLA[NE]
38	20 38 37.294	42 37 31.35	0.94	9.33	14	⋯
39	20 38 37.752	42 37 35.60	12.46	14.05	183	⋯
40	20 38 37.872	42 37 36.47	5.22	15.48	77	⋯

Notes.
[a] Positions and peak intensities of the ALMA 1.3 mm continuum sources determined from the images with a beam size of $0\farcs13 \times 0\farcs06$ (PA $= -2°$) and rms $\simeq$0.06 mJy beam^{-1} (see Section 3.1). The millimeter continuum sources are not resolved at FWHM, which implies physical sizes for the dust emission of $\lesssim$170 au. Positional uncertainties are $\sim0\farcs02$. The phase center is at α(J2000) $= 20^h38^m36\fs4860$, δ(J2000) $= 42°37'34\farcs090$.
[b] Peak intensities corrected by the primary beam.
[c] Distance from the source to the phase center of the observations.
[d] Total mass (dust+gas) from Equation (A2), assuming $T_{\rm dust} = 50$ K (see Appendix A), except for source ID 28 (VLA2), where we assume $T_{\rm dust} = 300$ K (see Section 4.1).
[e] The association with the millimeter cores MM1, MM2, MM3, MM[N], and/or the VLA sources VLA[SW], VLA1, VLA2, VLA3, VLA[NE] (Rodríguez-Kamenetzky et al. 2020) is indicated.
[f] The source proposed to power the highly collimated SiO bipolar outflow detected $\sim6''$ northeast of VLA2 (see Appendix C and Figure C1).

VLA2), assuming a density $n(H_2) \gtrsim (5 \times 10^5)$–$10^6$ cm^{-3}, and adopting a diameter size of $0\farcs5$ (650 au) from the emission image (Figure 2(a)), we roughly estimate a molecular mass $M(H_2) \gtrsim 4$–8×10^{-4} $M_\odot$. In addition, given its proximity to VLA2, we consider it plausible that this particular dense gas could be related to the obstacle predicted by Surcis et al. (2023) to halt the expanding motions of the H_2O masers observed to the northeast of VLA2 (see Figure 2 and the discussion in Section 4.2).

We also identify an H_2CO disk-like structure centered on VLA3 with a velocity gradient in the east–west direction (see Figure 2), and therefore perpendicular to the VLA3 radio jet oriented in the north–south direction (Carrasco-González et al. 2010; Rodríguez-Kamenetzky et al. 2020). In addition, the H_2CO line is seen in absorption toward VLA3 (absorption is also observed in SiO at this location; see Figure B1). These results on VLA3 will be presented and discussed in a forthcoming paper.

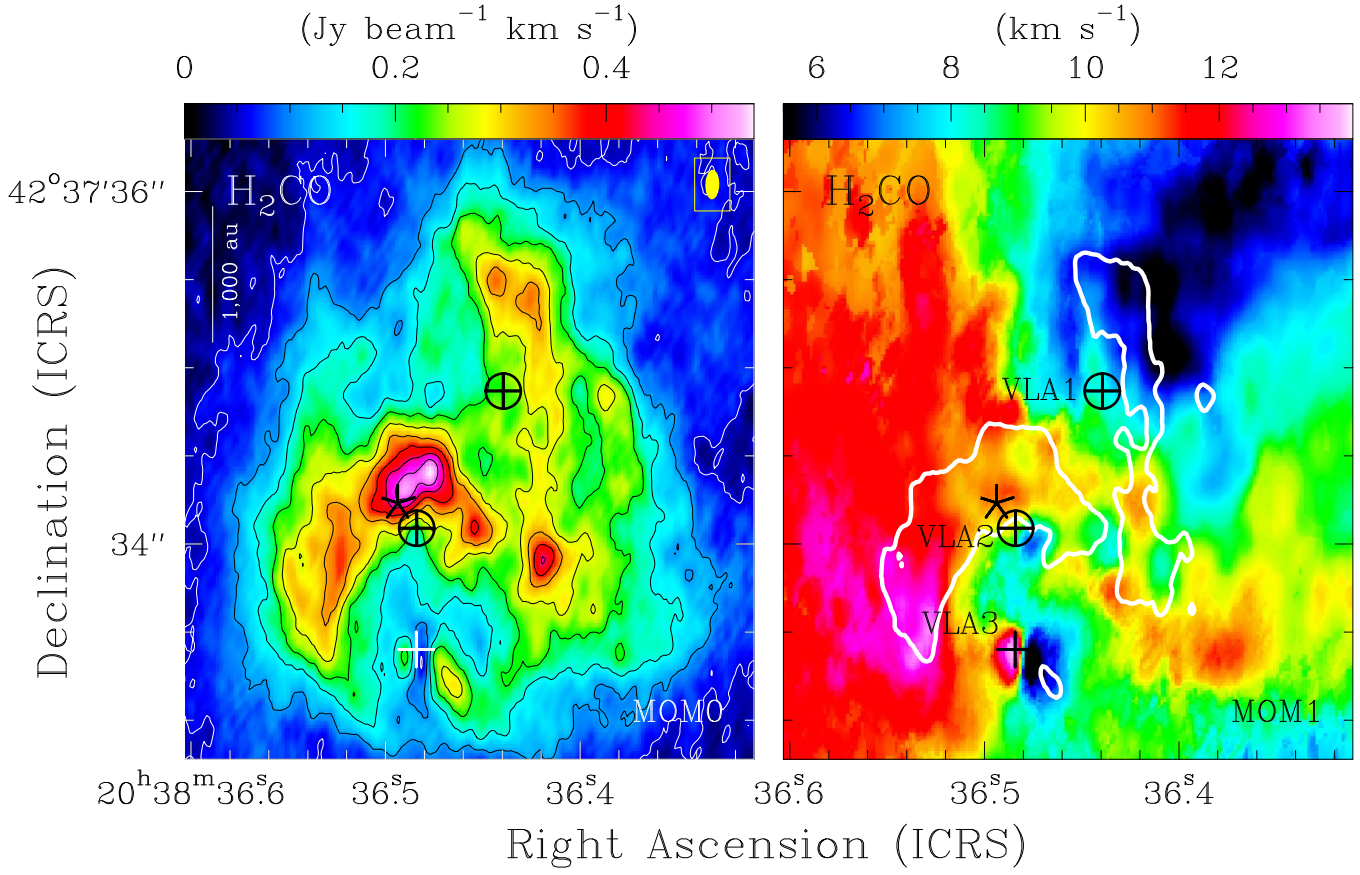

Figure 2. Left panel (a): Integrated intensity image (moment of order 0) of the H_2CO [3(0,3)-2(0,2)] emission line in the velocity range $V_{LSR} \simeq -4$ to $+23$ km s^{-1}. Contour levels are 10, 20, 30, 40, 50, 60, 70, 80, and 90 percent of the maximum integrated intensity of the image, 0.54 Jy beam^{-1} km s^{-1}. The synthesized beam is plotted as a yellow ellipse at the upper right corner of the image. Right panel (b): velocity field image (moment of order 1). To obtain this moment-1 image, we applied a 4σ threshold (4 mJy beam^{-1}) to the individual spectral channels. The white line traces the half-power contour of the MOM0 image in the left panel. Ringed cross symbols for VLA1 and VLA2 indicate that these are the activity centers of strong H_2O maser emission in the W75N(B) star-forming region (see, e.g., Surcis et al. 2023). The five-pointed star in both panels marks the location of the northeastern maser components in the VLA2 H_2O maser shell, where the expansion appears to have halted (Surcis et al. 2023).

3.3. General Distribution of the SiO Line Emission

The spatial and kinematic distribution of silicon monoxide emission is completely different from that of formaldehyde discussed in the previous section (Section 3.2). In Figure 3(a) we show the image of the integrated intensity of the SiO [$v = 0$, 5−4] emission line covering the same spatial region as that of H_2CO in Figure (2(a)). From the comparison of these two images (Figures 2(a) and 3(a)), we see that, while the H_2CO emission is distributed in several bright molecular clumps close, but not coinciding with any of the three massive protostars (VLA1, VLA2, and VLA3), the SiO emission is strongly and almost exclusively concentrated around VLA2. This remarkable behavior related to the strong concentration of SiO emission on VLA2 had already been reported by Minh et al. (2010) through SMA observations, but without resolving its spatial distribution. With our ALMA observations, we now resolve the SiO emission around VLA2 into a northwest–southeast elongated structure with a size of $\sim 0\farcs6 \times 0\farcs3$ ($\sim$780 au × 390 au; PA $\simeq -53°$), as seen in Figure 3(b). The range of velocities with SiO emission observed within this elongated structure surrounding VLA2 is $V_{LSR} \simeq -20$ to $+28$ km s^{-1}, which is significantly larger than that of H_2CO emission throughout all the region containing the three massive protostars (Section 3.2).

The SiO emission is a well-known tracer of shocked gas since the molecule is present in the gas phase in regions undergoing shocks with velocities of $\gtrsim$25 km s^{-1} (e.g., Schilke et al. 1997). Moreover, the SiO lines are high-density tracers and, for instance, the critical density of excitation for the SiO(5−4) transition is $\simeq 1.5 \times 10^6$ cm^{-3} (Huang et al. 2022). These extreme properties of the SiO excitation, together with the distribution of its emission described above, lead us to conclude the presence of very strong shocks around VLA2. We think that this is a consequence of the high outflow activity that VLA2 has, with very intense H_2O masers expanding at several tens of km s^{-1} driven by strong repetitive, short-lived ionized winds from the central source (Torrelles et al. 2003; Kim et al. 2013; Carrasco-González et al. 2015; Surcis et al. 2023). All these properties observed in VLA2 are what make this massive protostar unique in comparison with the other two massive protostars in the region (VLA1 and VLA3). In Section 4.1 we discuss and interpret the SiO structure with its kinematics in terms of a molecular toroid surrounding VLA2, together with a wide-angle outflow.

4. Discussion

4.1. The SiO Toroid Surrounding W75N(B)-VLA2

The elongated SiO structure ($\sim$780 au × 390 au, PA $\simeq -53°$; Section 3.3, Figure 3(b)) that surrounds VLA2 is approximately

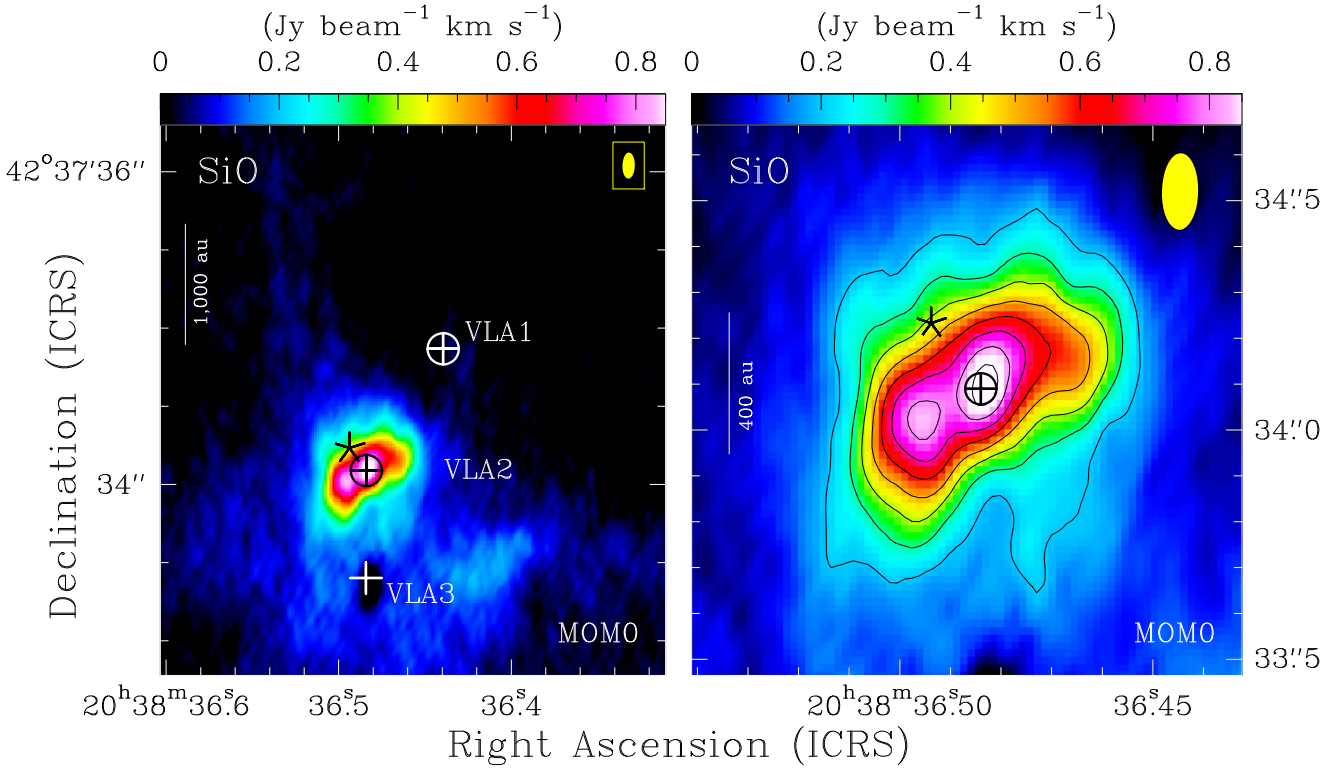

Figure 3. Left panel (a): Integrated intensity image (moment of order 0) of the SiO [$v = 0$, 5-4] emission line in the velocity range $V_{\rm LSR} \simeq -20$ to $+28$ km s^{-1}. The displayed field of view is the same as the one shown in Figure 2(a) for H_2CO. Right panel (b): zoom-in showing the integrated SiO emission around VLA2. Contour levels are 0.2, 0.3, 0.4, 0.5, 0.6, 0.7, 0.8, and 0.9 Jy beam^{-1} km s^{-1}. All symbols used in this figure are the same as those shown in Figure 2.

perpendicular to the major axis of the expanding H_2O maser shell (PA $\simeq 45°$; Surcis et al. 2014, 2023), which, in its turn, is shock-excited and driven by the VLA2 ionized jet (PA $\simeq 65°$; Carrasco-González et al. 2015). We interpret this SiO molecular structure as the toroid whose existence was hypothesized and modeled by Carrasco-González et al. (2015) as the collimating agent of an episodic, originally isotropic ionized wind associated with VLA2. These authors explain the observed evolution of a noncollimated outflow to a collimated outflow in VLA2 as being due to a toroidal environmental density stratification, seen almost edge-on, with densities $\sim 5 \times 10^7$ cm^{-3} at distances of $\sim$28 au from the central massive protostar. This seems to be consistent with the fact that SiO(5-4) emission, which traces densities $\gtrsim 1.5 \times 10^6$ cm^{-3}, is observed up to distances of $\sim$390 au from VLA2. Assuming this critical density of SiO as the minimum density for the entire toroid-like structure and given its observed size, a lower limit for the molecular mass $M(H_2) \gtrsim 2 \times 10^{-3}$ $M_\odot$ is estimated. An independent estimate for a lower limit of the total mass (gas+dust) in this region can be obtained from the observed dust continuum emission of the unresolved VLA2 source (see Appendix A), under the assumption of optically thin emission and using Equation (A2) (see Appendix A). Adopting $T_d = 300$ K (a reasonable value for gas temperatures near the massive object considering the presence of strong H_2O maser emission nearby, which implies that the gas should be at high temperatures), we obtain a total mass (gas+dust) $\gtrsim 5 \times 10^{-2}$ $M_\odot$ ($\gtrsim$51 M_J; Table A1).

Disk-like structures have been also reported in SiO emission surrounding other massive protostars (e.g., Gómez et al. 1999; Matthews et al. 2010; Maud et al. 2018). In particular, Maud et al. (2018), through ALMA 1.3 mm observations, report a rotating SiO disk and a disk wind from the massive protostar G17.64+0.16 (probably an O-type star). The radius of the SiO disk structure in that object extends up to $\sim$600 au, similar to that of the SiO toroid observed around VLA2 (in terms of nomenclature we refer to toroids as disk-like structures with a size of $\sim$1000 au). The very large velocity components observed in SiO within the VLA2 toroid ($V_{\rm LSR} \simeq -20$ to $+28$ km s^{-1}) are consistent with the velocities of the shocks needed to produce SiO as proposed by Maud et al. (2018) for the disk (toroid) of G17.64+0.16. Similarly to G17.64+0.16, the shocks in VLA2 may originate at the inner edge and surface interface of the toroid by the fast expansion of the ionized wind and outflow ($\gtrsim$30 km s^{-1}; Surcis et al. 2014; Carrasco-González et al. 2015).

Figure 4(a) shows the position–velocity (PV) diagram of the SiO emission along the major axis of the toroid-like structure (PA $= -53°$) with an averaging width of 0.″14 (selected to optimize the visualization of the SiO kinematics). A velocity gradient of $\sim$6 km s^{-1} is observed in the inner and most intense part of the SiO structure at angular scales of $\sim$0.″1 ($\sim$130 au), with the more blueshifted velocities to the northwest and the more redshifted velocities to the southeast. This velocity shift is in the same sense as the velocity shift observed northwest–southeast in H_2CO at larger scales ($\sim$4″, Figure 2(b); see also Minh et al. 2010) and in other molecular species (e.g., SO_2, CH_3OH; Rodríguez-Kamenetzky et al. 2020). If the observed velocity shift of 6 km s^{-1} is due to rotating motions at the inner parts ($\sim$130 au) of the toroid, those motions could be gravitationally bound by a central mass of $\sim 10\,M_\odot$ assuming Keplerian conditions, consistent with the expected mass of a B1-B0.5 spectral type star for VLA2 (Shepherd 2001). However, it seems clear that observations at submillimetre wavelengths, with higher angular resolution than currently available in this work, are needed to resolve in more detail the

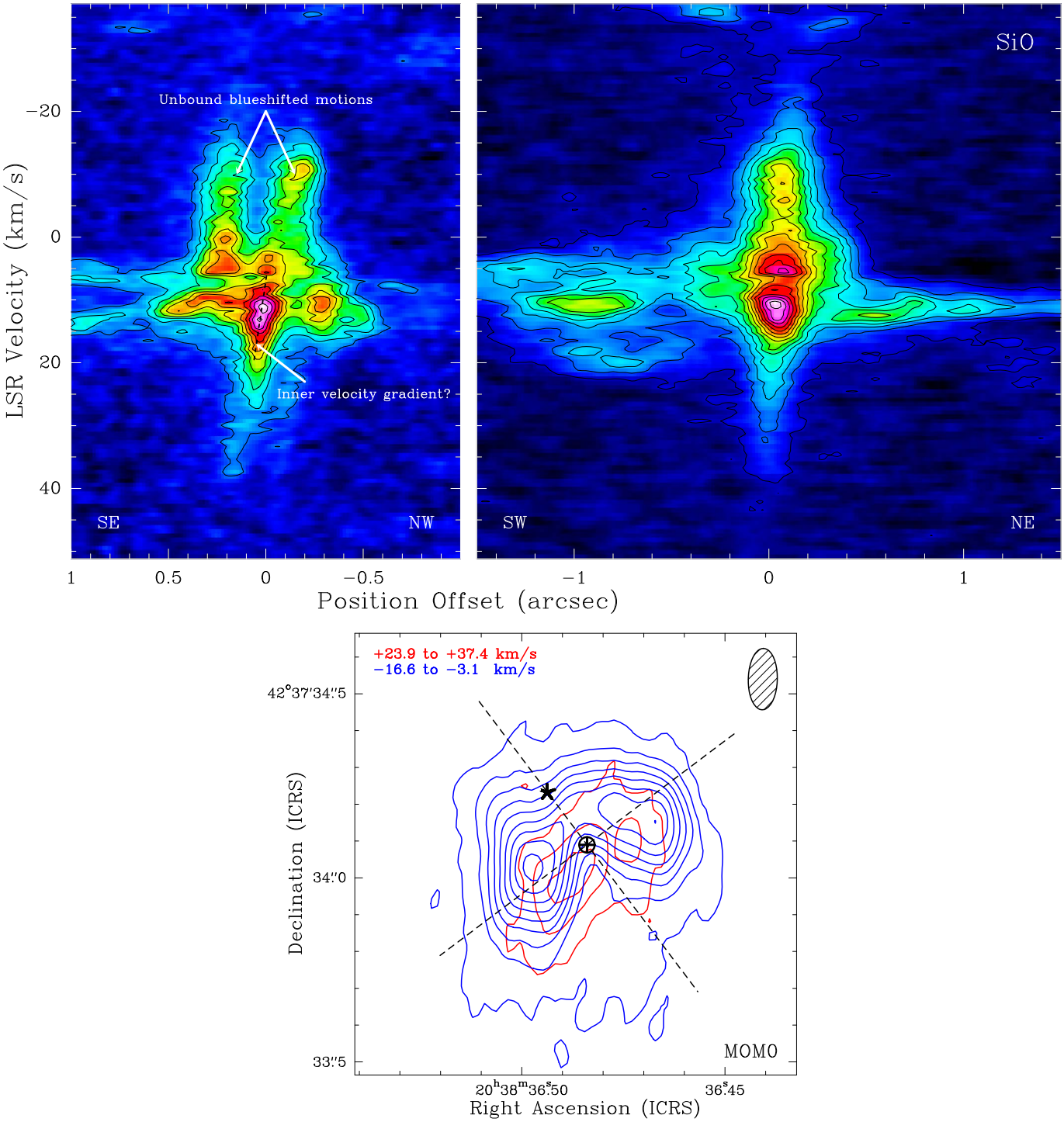

Figure 4. Diagrams and image showing the various velocity components of the VLA2 SiO toroid. Upper left panel (a): position–velocity diagram of the SiO emission along the major axis of the elongated structure (PA $\simeq -53°$; dashed line in Figure 4(c)) with an averaging width of $0\farcs14$. The first contour level and the increment step are 3σ, where $\sigma = 1.4$ mJy beam^{-1} (the rms of the diagram). The maximum of the diagram is 44 mJy beam^{-1}. The two "rabbit-ear-shaped" structures tracing unbound blueshifted motions are indicated. These structures originate from two peaks seen in the high-velocity blueshifted lobe (see Section 4.1 and Figure 4(c)). The dotted line indicates a possible inner velocity gradient in the SiO toroid. Upper right panel (b): same as upper left panel, but for the minor axis (PA $\simeq -143°$; dashed line in Figure 4(c) with an averaging width of $0\farcs6$. The first contour level is 3σ and the increment step is 6σ, where $\sigma = 0.38$ mJy beam^{-1}. The maximum of the diagram is 32 mJy beam^{-1}. Offset positions are with respect to the maximum SiO integrated intensity position (Figure 3(b)). Lower panel (c): integrated intensity image (moment of order 0) of the blueshifted and redshifted SiO in the high velocities ranges $V_{\rm LSR} = -16.6$ to -3.1 km s^{-1} and $V_{\rm LSR} = +23.9$ to $+37.4$ km s^{-1}, respectively. The first contour level is 4σ and the increment step is 6σ, where $\sigma = 5$ mJy beam^{-1} km s^{-1}. Symbols are as in Figure 2.

kinematic behavior of molecular gas in the internal parts of the toroid (at angular scales of $\lesssim 0\farcs1$).

The weakest SiO emission displays high blueshifted velocities, reaching up to $V_{\rm LSR} \simeq -17$ km s^{-1}, which appear as two rabbit-ear-shaped structures in the PV diagram along the major axis of the toroid (Figure 4(a)), and located symmetrically on both sides ($\sim \pm 0\farcs2$) of VLA2. Additionally, there is high redshifted velocity emission, with velocities up to

$V_{\rm LSR} \simeq +37$ km^{-1}, which is more apparent in the PV diagram along the minor axis of the SiO structure with an averaging width of 0.″6 (Figure 4(b)). To explain these motions, which amount to approximately 27 km s^{-1} relative to the ambient velocity ($V_{\rm LSR} = +10$ km s^{-1}; e.g., Surcis et al. 2023), and considering the distances of 0.″2 (260 au), a central mass of around 210 $M_\odot$ would be required. However, such a mass is not observed, leading us to conclude that these high velocities traced by the weakest SiO emission represent unbound motions of an outflow originating from the outer parts ($\sim \pm 0.''2$) of the toroid.

Figure 4(c) shows contour maps of the blueshifted ($V_{\rm LSR} = -16.6$ to -3.1 km s^{-1}) and redshifted ($V_{\rm LSR} = +23.9$ to $+37.4$ km s^{-1}) SiO integrated emission, with the blueshifted lobe being stronger than the redshifted one. This figure allows us to identify the source of the two rabbit-ear-shaped structures observed in Figure 4(a) as originating from the two peaks seen in the blueshifted lobe. These two peaks are separated by $\sim 0.''4$, with the VLA2 source located between them.

It is worth noting that the SiO blueshifted lobe is slightly displaced toward the northeast of VLA2, while the redshifted lobe is slightly displaced toward the southwest (Figure 4(c)). This displacement is consistent with the direction observed in the CO bipolar outflow at parsec scales (blueshifted to the northeast, redshifted to the southwest; e.g., Davis et al. 1998a, 1998b; Shepherd et al. 2003), indicating that the SiO outflow is being incorporated into the larger-scale molecular outflow, similar to the case of G17.64+0.16 (Maud et al. 2018). Furthermore, the morphological distribution of the two SiO outflow lobes (Figure 4(c)), which spatially surround VLA2, indicates the presence of a wide-angle outflow associated with this massive protostar.

Finally, we have considered the possibility that the two rabbit-ear-shaped structures that can be distinguished in Figure 4(a) are due to the presence of two protostars embedded in the SiO toroid, one of which is VLA2. However, the fact that no other continuum source is detected, despite the high sensitivity of the data, together with the distribution of the two SiO outflow lobes around VLA2, makes this possibility very unlikely.

4.2. A Wind Emerging from the Toroid, Interacting with a High-density Gas Obstacle

As mentioned above, Carrasco-González et al. (2015) showed that both the VLA2 radio continuum source and the maser shell around it evolved in ~20 yr from a compact source into an elongated one in the northeast–southwest direction. They successfully modeled this behavior as being due to the interaction of an episodic, short-lived isotropic ionized wind with a toroidal density stratification around the source. And we now find this toroidal structure, traced by the SiO emission.

Recently, Surcis et al. (2023) found that the northeast part of the shell traced by the H_2O masers has stopped, and they suggest that this is due to the interaction of the shell with a high-density gas obstacle. An analytical and numerical simulation of such a situation by Cantó et al. (2006) shows that, indeed, the interaction of a moving shell with a very dense medium can slow down the shell and stop its expansion completely. The detection of a strong H_2CO clump to the northeast of VLA2 as reported in the present paper (Section 3.2, Figure 2(a)) seems to be consistent with the suggestion of Surcis et al. (2023).

Following this idea, we can estimate the required gas density of the obstacle by assuming a balance between the thermal pressure of the gas in the clump and the ram pressure of the wind that drives the shell. That is,

$$nkT_k = \frac{\dot{M}_w V_w}{4\pi R^2}, \quad (1)$$

where n is the density of the obstacle, T_k its kinetic temperature, k the Boltzmann constant, $\dot{M}_w$ and V_w the mass-loss rate and terminal velocity of the isotropic wind, respectively, and R the distance between the observed halted H_2O masers and the powering source of the wind. Solving for the density of the clump we find

$$\left[\frac{n}{\rm cm^{-3}}\right] = 1.6 \times 10^9 \frac{\left[\frac{\dot{M}_w}{10^{-7} M_\odot {\rm yr}^{-1}}\right] \times \left[\frac{V_w}{100 \text{ km s}^{-1}}\right]}{\left[\frac{T_k}{10 \text{ K}}\right] \times \left[\frac{R}{100 \text{ au}}\right]^2}. \quad (2)$$

Assuming for $\dot{M}_w$ and V_w the values quoted above from Carrasco-González et al. (2015), together with $T_k = 300$ K and $R = 260$ au (~0.″2; Surcis et al. 2023), we found $n \simeq 3.5 \times 10^7$–3.0×10^8 cm^{-3}. This is a very high density, but consistent with the fact that this obstacle is located within a very high-density region, close to the observed H_2CO clump to the northeast of VLA2 (Figure 2(a)) and to the outer parts of the SiO toroid (Figure 3(b)). In addition, we should also consider that the density we estimated for the obstacle to halt the expanding motions of the H_2O masers to the northeast of VLA2 is likely to be an upper limit to the actual density. This is so because (1) we have calculated the gas pressure (left expression of Equation (1)) from the kinetic temperature only, but if the clump has turbulent motions (which is most likely the case; see Surcis et al. 2023) the actual pressure will be higher; (2) the ram pressure (right expression in Equation (1)) assumes that the shock is normal to the direction of the wind, but any deviation from this condition will produce a lower ram pressure; and (3) to estimate the density in Equation (2), we have used the projected distance between the obstacle and the source, but the actual linear distance might be longer.

5. Summary

Observations of the W75N(B) massive star-forming region using ALMA at a wavelength of 1.3 mm (beam = 0.″17 × 0.″08, PA = −2°) are presented, focusing on the continuum, H_2CO, and SiO lines. This region contains several massive protostars, including VLA1, VLA2, and VLA3, which are clustered within an area of ~2″ in size (~2600 au). The most relevant results are summarized as follows:

1. We detected 40 compact 1.3 mm continuum sources within an area of ~30″ diameter (~39,000 au), with three of them coinciding with VLA1, VLA2, and VLA3. The majority of these sources are new detections and are likely indicative of low- or intermediate-mass young stellar objects (YSOs).
2. The H_2CO emission is distributed in a clumpy structure around VLA1, VLA2, and VLA3. In contrast, the SiO emission is highly concentrated almost exclusively on

VLA2, implying the presence of intense shocks in the vicinity of this particular massive protostar. The SiO emission outlines an elongated structure that is perpendicular to the major axis of the wind-driven shell of H_2O masers and its associated radio jet. We identify this structure as the toroidal structure that was previously theorized to explain the outflow's evolution from an almost isotropic outflow to a collimated one.

3. The observations provide a plausible scenario in which we are observing a SiO toroid and a wide-angle outflow surrounding VLA2. The wide-angle SiO outflow originates from the outer regions of the toroid, being incorporated into the large-scale bipolar molecular outflow. The gas located in the inner regions of the toroid might be rotating, although more precise observations are required to confirm this.
4. The location of the obstacle that was previously predicted to stop the expansion of the wind-driven H_2O maser shell has been identified. It is situated between the outer parts of the SiO toroid and one of the main H_2CO clumps detected nearby, toward the northeast of VLA2. Additionally, this determination involves estimating the necessary gas density to impede the shell's expansion toward the northeast.

Acknowledgments

This paper makes use of ALMA data ADS/JAO. ALMA#2019.1.00059.S. ALMA is a partnership of ESO (representing its member states), NSF (USA) and NINS (Japan), together with NRC (Canada), MOST and ASIAA (Taiwan), and KASI (Republic of Korea), in cooperation with the Republic of Chile. The Joint ALMA Observatory is operated by ESO, AUI/NRAO and NAOJ. The data processing for this paper has been carried out using the Spanish Prototype of an SRC (SPSRC) service and support, funded by the Spanish Ministry of Science, Innovation and Universities, by the Regional Government of Andalusia, by the European Regional Development Funds and by the European Union NextGenerationEU/PRTR. J.C. acknowledges the support of DGAPA/UNAM (Mexico) project IG100422. C.C.-G. acknowledges support from UNAM DGAPA-PAPIIT grant IG101321 and from CONACyT Ciencia de Frontera project ID 86372. G.A. and J.F.G. acknowledge support from grants PID2020-114461GB-I00 and CEX2021-001131-S, funded by MCIN/AEI/10.13039/5011000110. J.M.G., A.S-M., and J.M.T. acknowledge partial support from the PID2020-117710GB-I00 grant funded by MCIN/AEI/10.13039/501100011033, and by the program Unidad de Excelencia María de Maeztu CEX2020-001058-M. A.S-M. also acknowledges support from the RyC2021-032892-I grant funded by MCIN/AEI/10.13039/501100011033 and by the European Union "Next GenerationEU"/PRTR. This work was partially supported by FAPESP (Fundação de Amparoá Pesquisa do Estado de São Paulo) under grant 2021/01183-8. J-S.K. acknowledges support from grant NSFC 11988101.

Facility: ALMA.

Software: CASA.

Appendix A
1.3 mm Continuum Sources

Table A1 lists the position of all the 1.3 mm continuum compact sources detected with ALMA in a region of $\sim 30''$ ($\sim$39,000 au) centered on the massive protostar W75N(B)-VLA2 (see Section 3.1). Peak flux densities are primary beam corrected. Their association (if any) with sources detected at other wavelengths is indicated in the last column of Table A1. Figure A1 shows the distribution of these millimeter continuum sources (indicated by crosses) together with the positions of the centimeter continuum sources detected with the VLA (Rodríguez-Kamenetzky et al. 2020). We are proposing, in particular, that one of these detected continuum sources (source ID 32 in Table A1) is the powering source of the highly collimated bipolar jet that we have detected $\sim 6''$ ($\sim$7800 au) northeast of VLA2 (see Appendix C and Figure C1).

Dust mass estimates in the detected sources can be obtained from the 1.3 mm continuum emission assuming that it is optically thin and that the dust is isothermal within the beam size, through the equation

$$M_{\rm dust} = \frac{S_\nu D^2}{\kappa_\nu B_\nu(T_{\rm dust})}, \quad \text{(A1)}$$

where S_ν is the observed flux density (Table A1), D the source distance (1.3 kpc), κ_ν the dust opacity, and $B_\nu(T_{\rm dust})$ the Planck function at the dust temperature $T_{\rm dust}$. Adopting a dust opacity $\kappa_\nu(1.3\ {\rm mm}) = 0.899\ {\rm cm^2\ g^{-1}}$ (Ossenkopf & Henning 1994; Diaz-Rodriguez et al. 2022), we obtain

$$M_{\rm dust} \simeq 1.4 \times 10^{-4} M_\odot \left[\frac{S_{1.3\ {\rm mm}}}{\rm mJy}\right] \times \left[\frac{T_{\rm dust}}{50\ {\rm K}}\right]^{-1}. \quad \text{(A2)}$$

These dust mass values should be taken with caution and as a first approximation, in particular because if the emission is not optically thin they represent lower limits. For sources with flux densities of $\sim$1 mJy (Table A1), and assuming a gas-to-dust ratio of 100, total masses (dust+gas) of $\sim 1.5 \times 10^{-2}\, M_\odot$ ($\sim 15\, M_J$) are estimated for $T_{\rm dust} = 50$ K, similar to the values obtained for protostellar disks of low-mass YSOs in massive star-forming regions, e.g., GGD 27 (Busquet et al. 2019), or Orion molecular clouds A and B (Tobin et al. 2020). This suggests that, in the W75N(B) massive star-forming region, there may also exist a significant population of low-mass YSOs (coexisting with massive protostars as VLA1, VLA2, and VLA3, and other possible intermediate-mass YSOs), having protostellar disks of size $\lesssim$170 au. Complementary observations at submillimeter wavelengths will indeed be important in properly characterizing and distinguishing the nature of these sources as potential protostars.

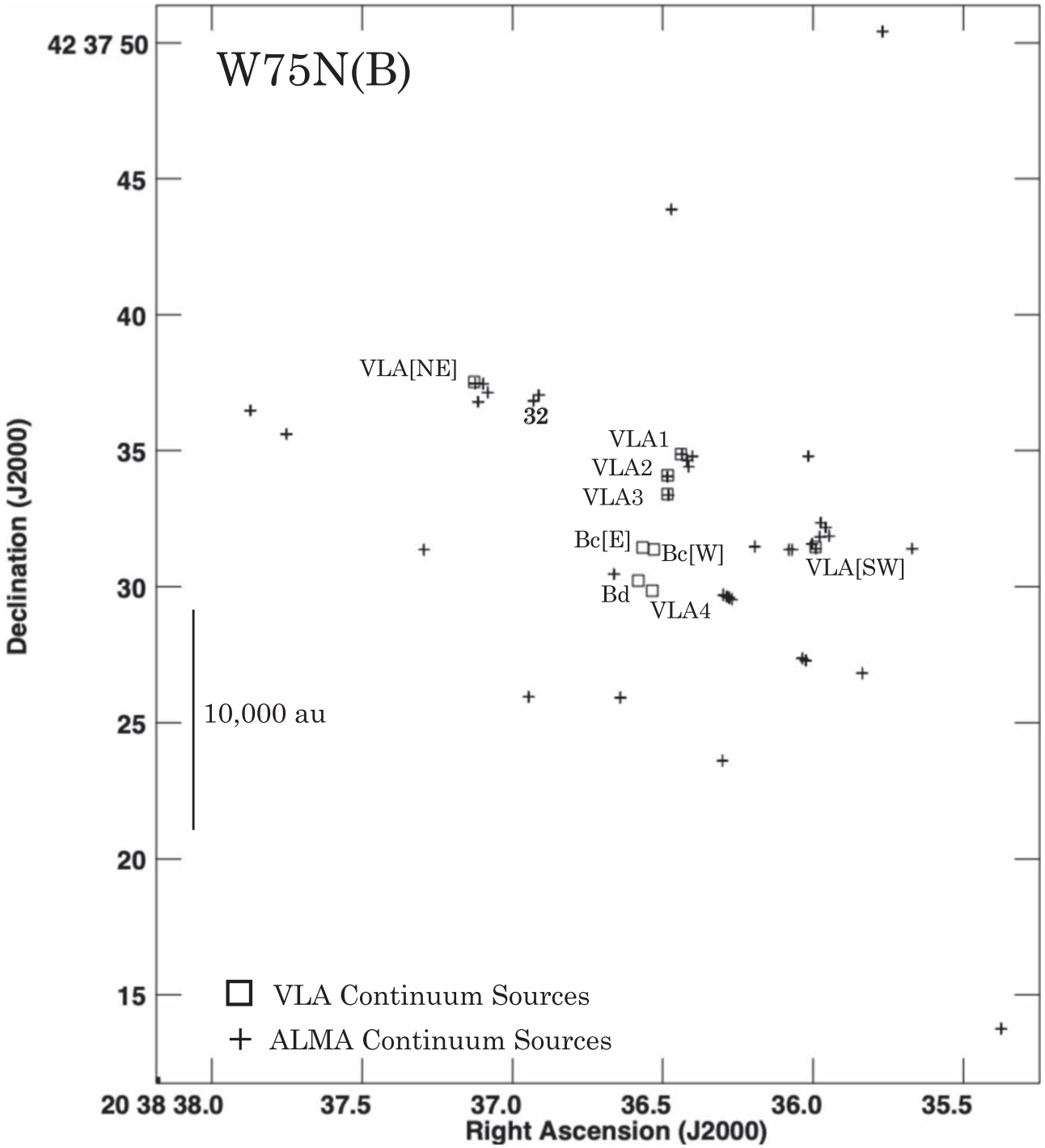

Figure A1. Spatial distribution of the 1.3 mm continuum sources detected in a region of ∼30″ in size. Their positions (indicated here by crosses) and flux densities are listed in Table A1. The powering source of the SiO bipolar jet also detected with our ALMA observations (see Appendix C and Figure C1) is labeled as number 32 (Table A1). This source is located in between the two lobes of the SiO bipolar jet (Figure C1). The positions of the VLA continuum sources (Rodríguez-Kamenetzky et al. 2020) are also labeled and indicated by squares.

Appendix B
H_2CO and SiO Absorption Lines Toward VLA3

H_2CO and SiO lines are seen in absorption against the continuum source VLA3. In Figure B1 we present the spectra at the location of this source. Both show an absorption feature centered at $V_{LSR} \simeq 6.4$ km s^{-1}.

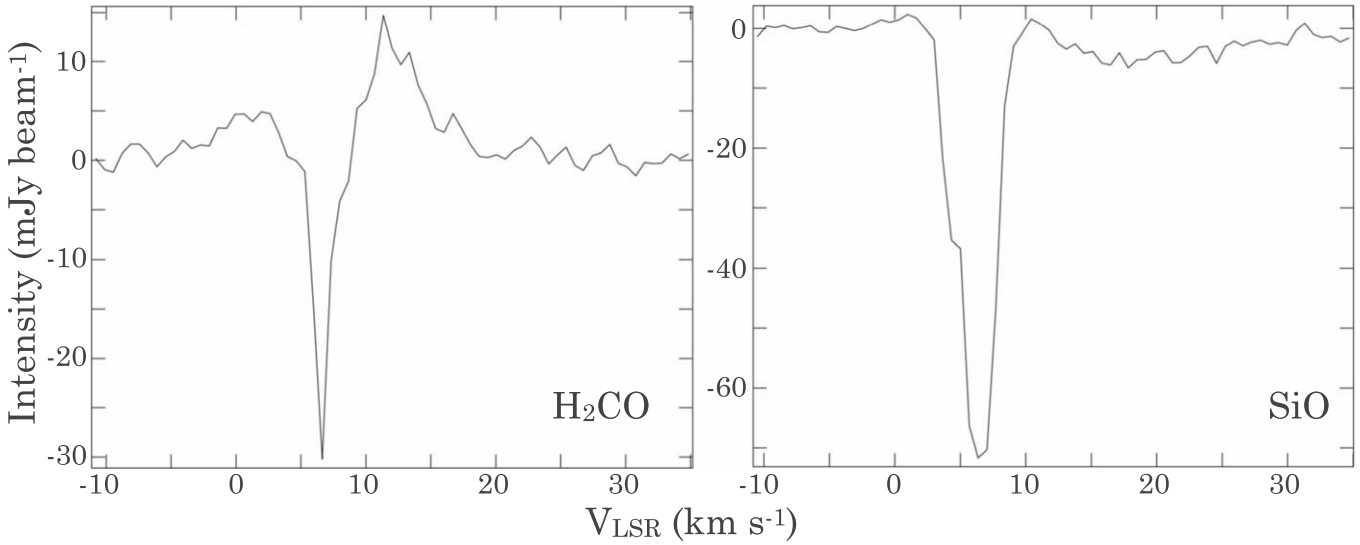

Figure B1. H_2CO (left panel) and SiO (right panel) lines seen in absorption toward the continuum source VLA3.

Appendix C
Highly Collimated Bipolar SiO Jet

We report here the detection of an extremely highly collimated bipolar SiO jet located ∼5″ (∼6500 au) northeast of the three massive protostars (Figure C1). This bipolar jet extends in the southeast–northwest direction, over an angular scale of ∼8″ (∼10,400 au) and velocities in the range $V_{\rm LSR} \simeq -3$ to +43 km s^{-1}. From the detected compact millimeter continuum sources in the W75N(B) region (Section 3.1), we identify one of them (source ID 32 in Table A1) that is well-centered between the two jet lobes (Figure C1) as the most probable powering source, most likely a low-mass protostar. Since it is located in a region outside the main focus of our observations on VLA2, we will present and discuss the main properties of this remarkable bipolar SiO jet in a forthcoming paper.

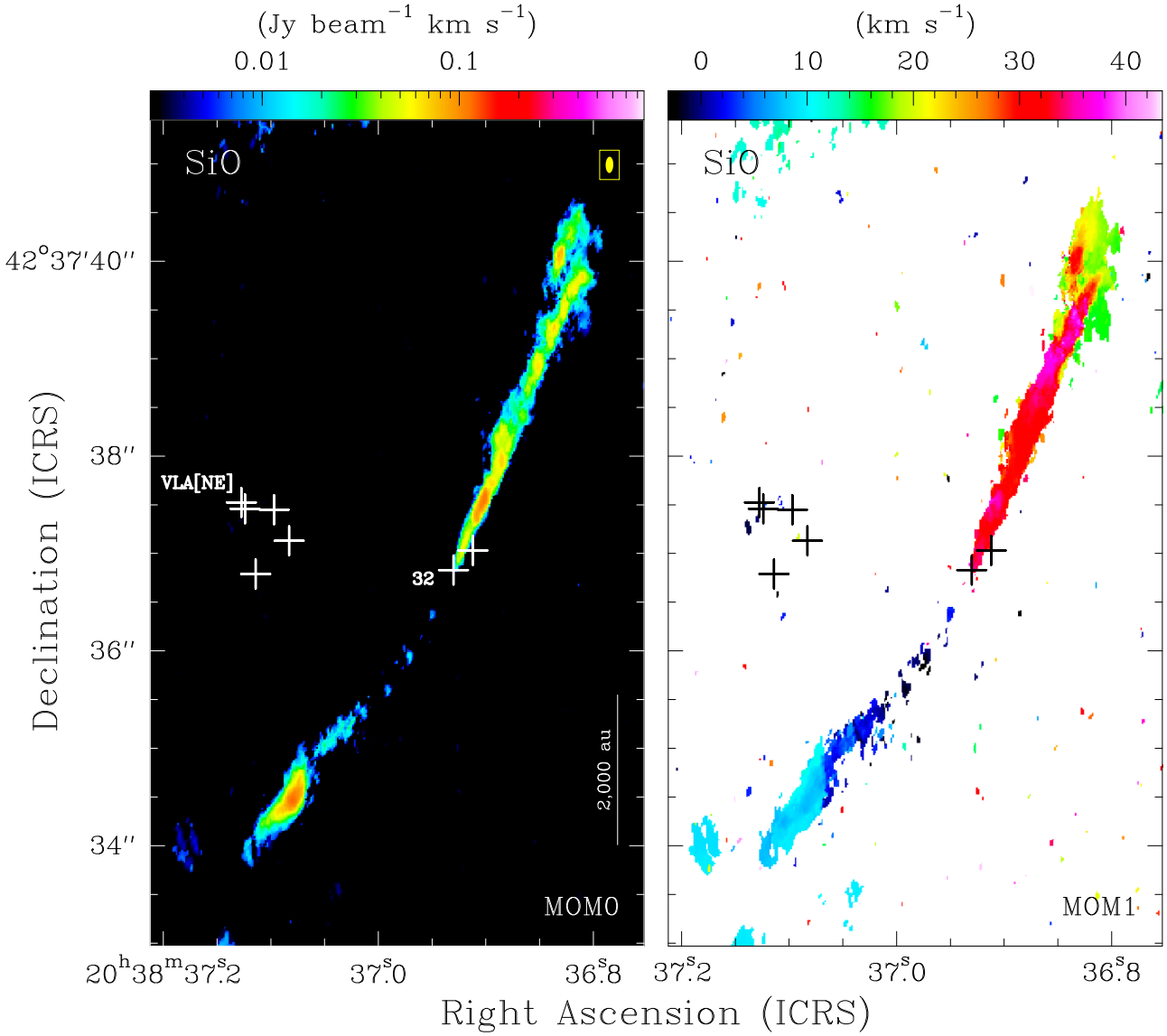

Figure C1. Left panel: integrated intensity image (moment of order 0) of the SiO bipolar jet found ∼5″ northeast of VLA2 in the velocity range $V_{LSR} \simeq -3$ to +43 km s^{-1}. The position of the 1.3 mm continuum source proposed to power this SiO jet (Appendix C, Table A1) is indicated by a cross and labeled as number 32. The nearby radio continuum source VLA[NE] (Rodríguez-Kamenetzky et al. 2020) is also labeled. Other 1.3 mm continuum sources found nearby of the SiO jet are also indicated by crosses. The synthesized beam is marked as a filled yellow ellipse at the upper right corner. Right panel: velocity field image of the SiO jet (moment of order 1).

ORCID iDs

José F. Gómez https://orcid.org/0000-0002-7065-542X
José M. Torrelles https://orcid.org/0000-0002-6896-6085
Josep M. Girart https://orcid.org/0000-0002-3829-5591
Gabriele Surcis https://orcid.org/0000-0003-2775-442X
Jeong-Sook Kim https://orcid.org/0000-0002-4987-5540
Jorge Cantó https://orcid.org/0000-0003-3863-7114
Guillem Anglada https://orcid.org/0000-0002-7506-5429
Salvador Curiel https://orcid.org/0000-0003-4576-0436
Wouter H. T. Vlemmings https://orcid.org/0000-0002-2700-9916
Carlos Carrasco-González https://orcid.org/0000-0003-2862-5363
Adriana R. Rodríguez-Kamenetzky https://orcid.org/0000-0002-4731-4934
Soon-Wook Kim https://orcid.org/0000-0002-0978-4775
Ciriaco Goddi https://orcid.org/0000-0002-2542-7743
Huib J. van Langevelde https://orcid.org/0000-0002-0230-5946
Álvaro Sanchez-Monge https://orcid.org/0000-0002-3078-9482

References

Añez-López, N., Osorio, M., Busquet, G., et al. 2020, ApJ, 888, 41
Bartkiewicz, A., Sanna, A., Szymczak, M., et al. 2020, A&A, 637, A15
Busquet, G., Girart, J. M., Estalella, R., et al. 2019, A&A, 623, L8
Cantó, J., Raga, A. C., & Adame, L. 2006, MNRAS, 369, 860
Carrasco-González, C., Rodríguez, L. F., Torrelles, J. M., Anglada, G., & González-Martín, O. 2010, AJ, 139, 2433
Carrasco-González, C., Sanna, A., Rodríguez-Kamenetzky, A., et al. 2021, ApJL, 914, L1
Carrasco-González, C., Torrelles, J. M., Cantó, J., et al. 2015, Sci, 348, 114
CASA Team, Bean, B., Bhatnagar, S., et al. 2022, PASP, 134, 114501
Davis, C. J., Moriarty-Schieven, G., Eislöffel, J., Hoare, M. G., & Ray, T. P. 1998a, AJ, 115, 1118

Davis, C. J., Smith, M. D., & Moriarty-Schieven, G. H. 1998b, MNRAS, 299, 825
Diaz-Rodriguez, A. K., Anglada, G., Blázquez-Calero, G., et al. 2022, ApJ, 930, 91
Girart, J. M., Fernández-López, M., Li, Z. Y., et al. 2018, ApJL, 856, L27
Goddi, C., Ginsburg, A., Maud, L. T., Zhang, Q., & Zapata, L. A. 2020, ApJ, 905, 25
Gómez, J. F., Sargent, A. I., Torrelles, J. M., et al. 1999, ApJ, 514, 287
Huang, K. Y., Viti, S., Holdship, J., et al. 2022, A&A, 666, A102
Hunter, T. R., Taylor, G. B., Felli, M., & Tofani, G. 1994, A&A, 284, 215
Jiménez-Serra, I., Martín-Pintado, J., Rodríguez-Franco, A., et al. 2007, ApJL, 661, L187
Kim, J.-S., Kim, S.-W., Kurayama, T., et al. 2013, ApJ, 767, 86
Mangum, J. G., & Wootten, A. 1993, ApJS, 89, 123
Matthews, L. D., Greenhill, L. J., Goddi, C., et al. 2010, ApJ, 708, 80
Maud, L. T., Cesaroni, R., Kumar, M. S. N., et al. 2018, A&A, 620, A31
Minh, Y. C., Su, Y. N., Chen, H. R., et al. 2010, ApJ, 723, 1231
Ossenkopf, V., & Henning, T. 1994, A&A, 291, 943
Patel, N. A., Curiel, S., Sridharan, T. K., et al. 2005, Natur, 437, 109
Rodríguez-Kamenetzky, A., Carrasco-González, C., Torrelles, J. M., et al. 2020, MNRAS, 496, 3128
Rygl, K. L. J., Brunthaler, A., Sanna, A., et al. 2012, A&A, 539, A79
Sanna, A., Moscadelli, L., Surcis, G., et al. 2017, A&A, 603, A94
Schilke, P., Walmsley, C. M., Pineau des Forets, G., & Flower, D. R. 1997, A&A, 321, 293
Shepherd, D. S. 2001, ApJ, 546, 345
Shepherd, D. S., Testi, L., & Stark, D. P. 2003, ApJ, 584, 882
Shirley, Y. L. 2015, PASP, 127, 299
Surcis, G., Vlemmings, W. H. T., Goddi, C., et al. 2023, A&A, 673, A10
Surcis, G., Vlemmings, W. H. T., van Langevelde, H. J., et al. 2014, A&A, 565, L8
Tobin, J. J., Sheehan, P. D., Megeath, S. T., et al. 2020, ApJ, 890, 130
Torrelles, J. M., Gómez, J. F., Rodríguez, L. F., et al. 1997, ApJ, 489, 744
Torrelles, J. M., Patel, N. A., Anglada, G., et al. 2003, ApJL, 598, L115
Torrelles, J. M., Patel, N. A., Gómez, J. F., et al. 2001, Natur, 411, 277
van der Walt, S. J., Kristensen, L. E., Jørgensen, J. K., et al. 2021, A&A, 655, A86
Zeng, L., Zhang, Q., Alves, F. O., et al. 2023, ApJ, 954, 99